Earth, Planets and Space

FULL PAPER Open Access

Assessing the potential of ionosonde for forecasting post-sunset equatorial spread F: an observational experiment in Southeast Asia

Prayitno Abadi[1,2], Umar Ali Ahmad[2*], Yuichi Otsuka[3], Punyawi Jamjareegulgarn[4], Alif Almahi[5], Septi Perwitasari[6], Slamet Supriadi[7], Wendi Harjupa[1,2] and Reza Rendian Septiawan[2]

Abstract

The occurrence of equatorial spread F (ESF) has the potential to detrimentally impact space-based technological systems. This study investigates the utility of ionosondes in forecasting the incidence of post-sunset ESF in the zonal direction, utilizing observational data obtained from four ionosondes located near the magnetic Equator in Southeast Asia. Data were collected during the equinox seasons (March–April and September–October) between 2003 and 2020. To establish a relationship between the probability of post-sunset ESF occurrence and the evening vertical plasma drift (v), a logistic regression model was employed. Post-sunset ESF occurrence is defined as the presence of ESF during the time window between 19:00 and 21:00 LT, while v is derived from the average time derivative of virtual heights during the interval from 18:30 to 19:00 LT. Results indicate that the probability of post-sunset ESF occurrence approaches zero, signifying that ESF is unlikely to develop when v is negative. Conversely, when v exceeds 30 m/s, the probability of post-sunset ESF occurrence surpasses 0.87, indicating that ESF occurs almost invariably. The likelihood of post-sunset ESF occurrence reaches 1 when v equals or exceeds 40 m/s. Utilizing this model, the study determined that a single ionosonde positioned at the Equator can effectively forecast the incidence of post-sunset ESF up to a longitudinal distance of 30° from its location. The accuracy of ionosondes in predicting post-sunset ESF occurrence above their respective locations is approximately 0.80, with a 10% decrease in accuracy when forecasting ESF occurrence at longitudinal distances of 30°. In conclusion, this study enhances our understanding of the link between the evening vertical plasma drift and the manifestation of post-sunset ESF by leveraging ionosonde data. Furthermore, it provides valuable insights into the recommended coverage range of ionosondes for predicting post-sunset ESF occurrence in the zonal direction, which can be employed to fortify regional space weather services.

Keywords Equatorial spread F, Ionosonde, Logistic regression, Space weather services, Observational study

*Correspondence:
Umar Ali Ahmad
umar@telkomuniversity.ac.id
Full list of author information is available at the end of the article

Graphical Abstract

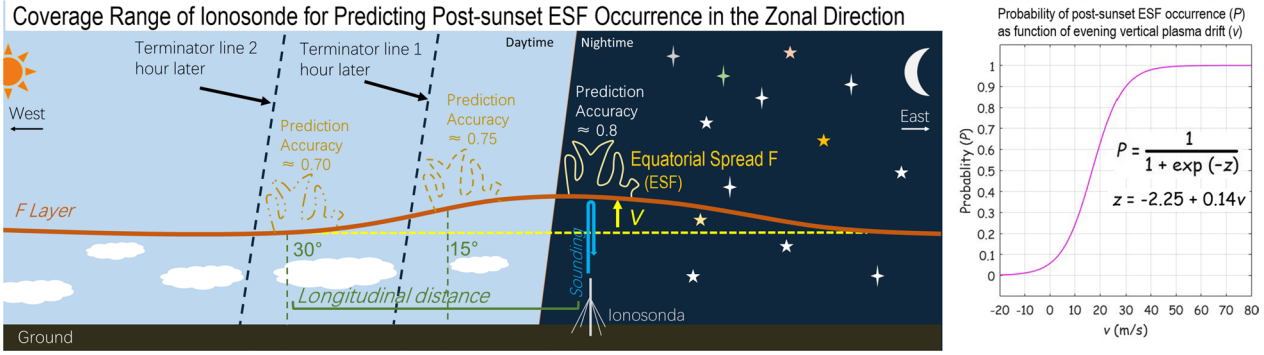

Introduction

Equatorial spread F, or ESF, is characterized by the dispersal of echoes observed in the F region trace of ionograms recorded by ionosondes in the equatorial zone, especially during nighttime. These echoes serve as indicators of ionospheric irregularities within the F-region ionosphere above the ionosonde site (Booker and Wells 1938). The origin of these irregularities lies in the Rayleigh–Taylor instability at the lower part of the F-region, which can subsequently propagate and nonlinearly develop into the topside, culminating in the formation of equatorial plasma bubble (EPB) (Woodman and La Hoz 1976). Comprehending the occurrence of ESFs is of paramount importance for space weather services, as they can exert significant influence on space-based communication and navigation systems (Ishii et al. 2021). These ionospheric irregularities, particularly those with spatial scales in the hundreds of meters, can induce scintillation on the GHz radio frequencies utilized in the Global Navigation Satellite System (GNSS), resulting in signal intensity fluctuations and, in some cases, signal loss (Seo et al. 2009). Consequently, accurate and timely information on ESFs is imperative for mitigating their impact on space-based technological systems.

Ionosondes have assumed a pivotal role in furnishing precise and timely data concerning ESFs in the realm of space weather services (Maruyama et al. 2007; Li et al. 2021; Patra and Das 2023). The measurement of vertical ion drift in the evening sector, obtained from ionosonde data, serves as an effective indicator of ESF activity (Anderson et al. 2004; Fagundes et al. 1999; Abadi et al. 2022). By monitoring variations in vertical drift, ionosondes can offer early alerts regarding ESF activity and contribute to the anticipation of the onset, duration, and intensity of these events.

A single ionosonde, however, can solely furnish information about the ionosphere directly above its location. ESFs may arise at any longitude along the magnetic Equator (Li et al. 2016). Therefore, an ionosonde situated at a specific position cannot be employed to forecast ESF occurrences at other longitudes (Saito and Maruyama 2007; Das et al. 2022). To effectively monitor and predict ESF generation at various longitudes, the deployment of multiple ionosondes is requisite. Nevertheless, the number of ionosondes and their spacing is often constrained by numerous factors, including suitable locations for instrumentation, deployment costs, logistical considerations, geographical constraints, and available funding and resources. These limitations in ionosonde site spacing present a formidable challenge in the prediction and monitoring of ESF activity. Consequently, it is imperative to investigate the optimal coverage area for a single ionosonde in forecasting ESF occurrences, with a crucial consideration being the effective range over which a single ionosonde can accurately predict ESF occurrences at other points. This underscores the necessity for precise and dependable information on ionospheric conditions, particularly in regions where ionosonde locations are unevenly distributed, to support regional space weather services.

This study assesses the ability of ionosondes to predict post-sunset ESF occurrences in Southeast Asia. The investigation will utilize an observational experiment conducted with the ionosonde network in Southeast Asia, comprised four ionosondes, to explore the extent to which one ionosonde situated along the magnetic Equator can optimally forecast ESF occurrences at other longitudes in the zonal (East–West) direction. Finally, the study will deliberate on the utilization of existing ionosondes in Southeast Asia to bolster

operational space weather services, particularly in forecasting ESF occurrences within the region.

Experimental setup

This study utilized three ionosondes from the Southeast Asia Low-latitude Ionospheric Network (SEALION) project (Maruyama et al. 2007), positioned strategically in Chumphon (CPN; 99.4°E, 10.7°N, magnetic latitude/MLAT: 1.3°N) in Thailand, Bac Lieu (BCL; 105.7°E, 9.3°N, MLAT: 1.5°N) in Vietnam, and Cebu (CEB; 123.9°E, 10.4°N, MLAT: 3.0°N) in the Philippines. Additionally, an ionosonde from the Global Ionosphere Radio Observatory (GIRO) network in Guam (GUM; 144.9°E, 13.6°N, MLAT: 5.6°N) was incorporated (Reinisch and Galkin 2011). Figure 1 illustrates the locations of these four ionosondes in proximity to the magnetic Equator (denoted by a blue dashed line) within the Southeast Asian sector. The longitudinal range between the westernmost and easternmost ionosondes, CPN and GUM, spans 45.46°, while the closest separation, CPN and BCL, measures 6.30°. Despite the non-uniform distribution of ionosonde locations due to geographical constraints, Southeast Asia represents one of the limited equatorial and low-latitude regions suitable for ground-based measurements in ESF research. Early studies by Fukao et al. (2003) utilizing the 47 MHz Equatorial Atmosphere Radar (EAR), Saito and Maruyama et al. (2007) employing SEALION ionosondes, and Thampi et al. (2009) using a satellite beacon network laid the foundation for ESF research in this region. Subsequent studies by Povero et al. (2015, 2017) and Abadi et al. (2017, 2021) extended the exploration of ESFs in this region.

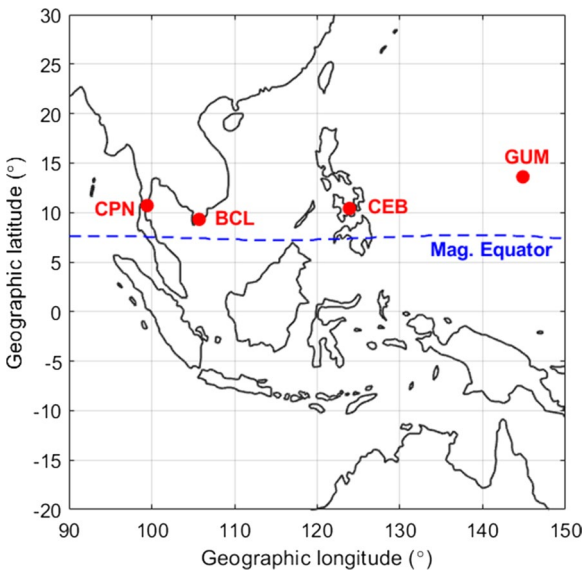

Fig. 1 Locations of four ionosondes used in this study, situated near the magnetic Equator

In this investigation, data from the virtual height of the F-region in the evening (h') at a frequency of approximately 3 MHz, along with the observation of ESF on ionograms obtained from ionosonde observations, were utilized. A 5-min temporal resolution was applied for manual h' scaling and visual observation of ESF occurrences in the SEALION ionosondes, while a 15-min resolution was employed for the GUM ionosonde. The study aims to evaluate the ionosondes' capacity to predict post-sunset ESF by examining the relationship between the vertical plasma drift in the evening equatorial region and the probability of post-sunset ESF occurrence. The methodology employed in this study aligns with Abadi et al. (2022), using logistic regression to model the probability of post-sunset ESF occurrence as a function of the evening vertical plasma drift.

To derive the evening vertical drift, data from the h' at ~3 MHz of the ionosonde data are used, and the appearance of ESF on the ionograms is used to determine the day with or without the occurrence of post-sunset ESF. To estimate the evening vertical drift on a specific day, we calculate the average time derivative of h' (dh'/dt) between 18:30 and 19:00 local time (LT). This time window falls within the pre-reversal enhancement (PRE) period (Huang and Hairston 2015; Olla et al. 2020). The PRE phenomenon involves an increase in the eastward electric field over the magnetic Equator before its transition to a westward direction (Farley et al. 1986; Eccles 1998). While the vertical drift observed at a single ionosonde site may not entirely represent PRE (Tsunoda et al. 2018), the vertical drift during the 18:30–19:00 LT interval is attributable to the influence of a zonal electric field, regardless of its origin. Additionally, vertical drift calculations were refrained from when ESF was evident on the ionogram as it distorts the F-layer trace, hindering accurate scaling of h' difficult. In cases where ESF emerged before or at 19:00 LT, the vertical drift was still calculated using the average dh'/dt during the 30 min leading up to the onset of ESF on the ionogram.

Determining post-sunset ESF occurrence or non-occurrence on a given day relied on visual inspection of ionograms between 19:00 and 21:00 LT for the presence of mixed spread-F (MSF), range spread-F (RSF), and frequency spread-F (FSF) types. Definitions for RSF, FSF, and MSF were based on the Union Radio-Scientifique Internationale (URSI) Handbook of Ionogram Interpretation and Reduction (Piggott and Rawer 1972). RSF identification involved discerning a broadening in range or virtual height in the lower segment of the F-layer trace on the ionogram. For FSF, the ionogram exhibited broadening of the F-layer trace in frequency

near the critical frequency (foF2). MSF, on the other hand, combined both RSF and FSF characteristics. In the absence of MSF, RSF, or FSF in the ionograms during the 19:00–21:00 LT timeframe, the non-occurrence of post-sunset ESF on that specific day was confirmed. It is important to note that ESF appearances during this 19:00–21:00 LT interval constitute post-sunset ESF occurrences in this study.

The 2-h timeframe for ESF observation (from 19:00 to 21:00 LT) was chosen to precisely establish the relationship between post-sunset ESF generation and evening vertical drift. ESFs can emerge at any longitude following local sunset and subsequently propagate eastward or westward at the same velocity as the ambient plasma. By observing ESFs within this specific time frame, ESF generation can be confined to the region directly above or in close proximity to the ionosonde's longitude. Given the zonal velocity of ESFs (approximately 100 m/s), this 2-h period effectively limits ESF generation to a longitudinal span of roughly 6°. In contrast, observing ESF occurrences over a longer timeframe would not only capture recently generated ESF directly above the ionosonde's location, but also those originating from longitudes to the east or west. This extended observation period could potentially distort the model of the probability of ESF occurrence in relation to evening vertical drift. This approach aligns with the method employed by Huang and Hairston (2015) to explore the connection between ESF generation and PRE.

Within this section, we provide examples of ESF appearances based on our observations, as illustrated in Fig. 2. The left (Fig. 2a, c, e, g) and right (Fig. 2b, d, f, h) panels in the figure correspond to data collected from SEALION (CPN and CEB) and GIRO (GUM) ionosondes, respectively. The presence of RSF, characterized by the broadening of the lower portion of the F-layer trace, is evident in Fig. 2a, b. In Fig. 2b, multireflection (2F, 3F, and 4F) of the F-layer trace is observed, and ESF appearances are not identified from these multireflection traces. Figure 2c, d illustrates instances of FSF, where the trace widens near the foF2. Additionally, the examples include demonstrations of MSF appearances on the ionogram, as demonstrated in Fig. 2e, f. In addition to RSF, FSF, and MSF, our observations of ESF appearances also reveal a strong RSF presence characterized by an extensive ESF echo range that extends well beyond the foF2 of the F-layer, encompassing the entire frequency range. Notably, the strong RSF commonly follows the occurrence of RSF, FSF, or MSF. In this study, post-sunset ESF occurrence on a specific day is defined based on the presence of ESF appearances (RSF, FSF, or MSF) in at least one ionogram between 19:00 LT and 21:00 LT. Conversely, non-occurrence of post-sunset ESF indicates that no ionogram exhibits ESF appearance during that specific period.

The probability of post-sunset ESF occurrence, as a function of the evening vertical drift based on observation, is modeled using logistic regression, expressed as $P=1/[1+\exp(-z)]$, where $z=\beta_0+\beta_1 v$. In this equation, P represents the logistic regression denoting the probability of post-sunset ESF occurrence, while z is a linear function comprising v, which signifies the evening vertical drift derived from the ionosonde, and β_0 and β_1 are the regression coefficients. Huang and Hairston (2015) previously demonstrated that the relationship between ESF occurrence and evening vertical drift can be effectively represented as a probability event, with the probability ranging between 0 and 1. Logistic regression is well-suited for capturing this probabilistic characteristic, with the coefficients β_0 and β_1 determined using the gradient descent technique, as detailed in Abadi et al. (2022).

This study collected data from all four ionosondes, resulting in 2690 observation days. The data encompass information on evening vertical drift and the occurrence or non-occurrence of post-sunset ESFs during the equinox seasons (March–April and September–October) from 2003 to 2020. It is noteworthy that the equinox season is recognized as the post-sunset ESF season in the Southeast Asian sector (Burke et al. 2004; Kil et al. 2009). The significant vertical drift during the PRE phenomenon arises from the alignment of the solar terminator with the geomagnetic meridian (Abdu et al. 1981, 1992; Su et al. 2008; Kil and Oh 2011), effectively triggering post-sunset ESF formation. This alignment primarily occurs during the equinox seasons in Southeast Asia.

Data were gathered from four ionosondes, specifically CPN, BCL, CEB, and GUM, for a total of 2690 days. CPN contributed 685 observation days, BCL had 739, CEB had 720, and GUM had 546. Out of these 2690 days, 1023 featured post-sunset ESF occurrences, while 1667 did not. Figure 3 provides the annual distribution of observation days for each station, encompassing days with and without post-sunset ESF occurrences. Remarkably, ESF appearances on ionograms predominantly occurred after 19:00 LT, accounting for 95% of cases, with the peak occurrence observed between 19:00 and 20:00 LT. Following 20:00 LT, the incidence of ESF appearances on ionograms decreased. The distribution of onset ESF appearances concerning evening vertical drift (v) is depicted in Fig. 3f, showing a tendency for onset ESF appearances to occur earlier (before 20:00 LT) when v is stronger.

P and z were obtained from the dataset comprising 2690 observation days. These parameters are used to quantitatively assess the ionosonde's performance in predicting the occurrence of post-sunset ESFs above the

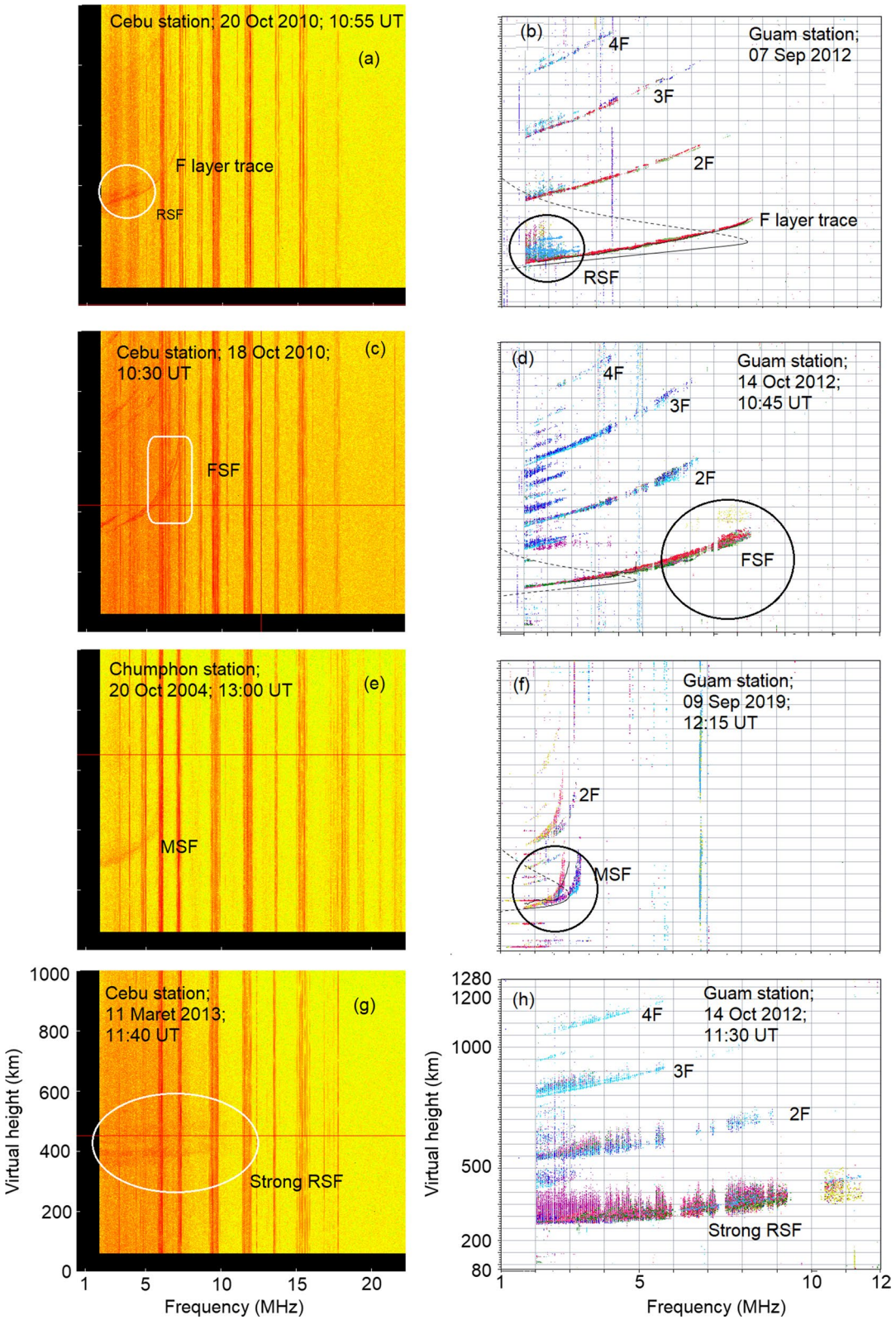

Fig. 2 Samples of equatorial spread F (ESF) appearance (RSF, FSF, and MSF) on the ionograms from ionosondes used in this study

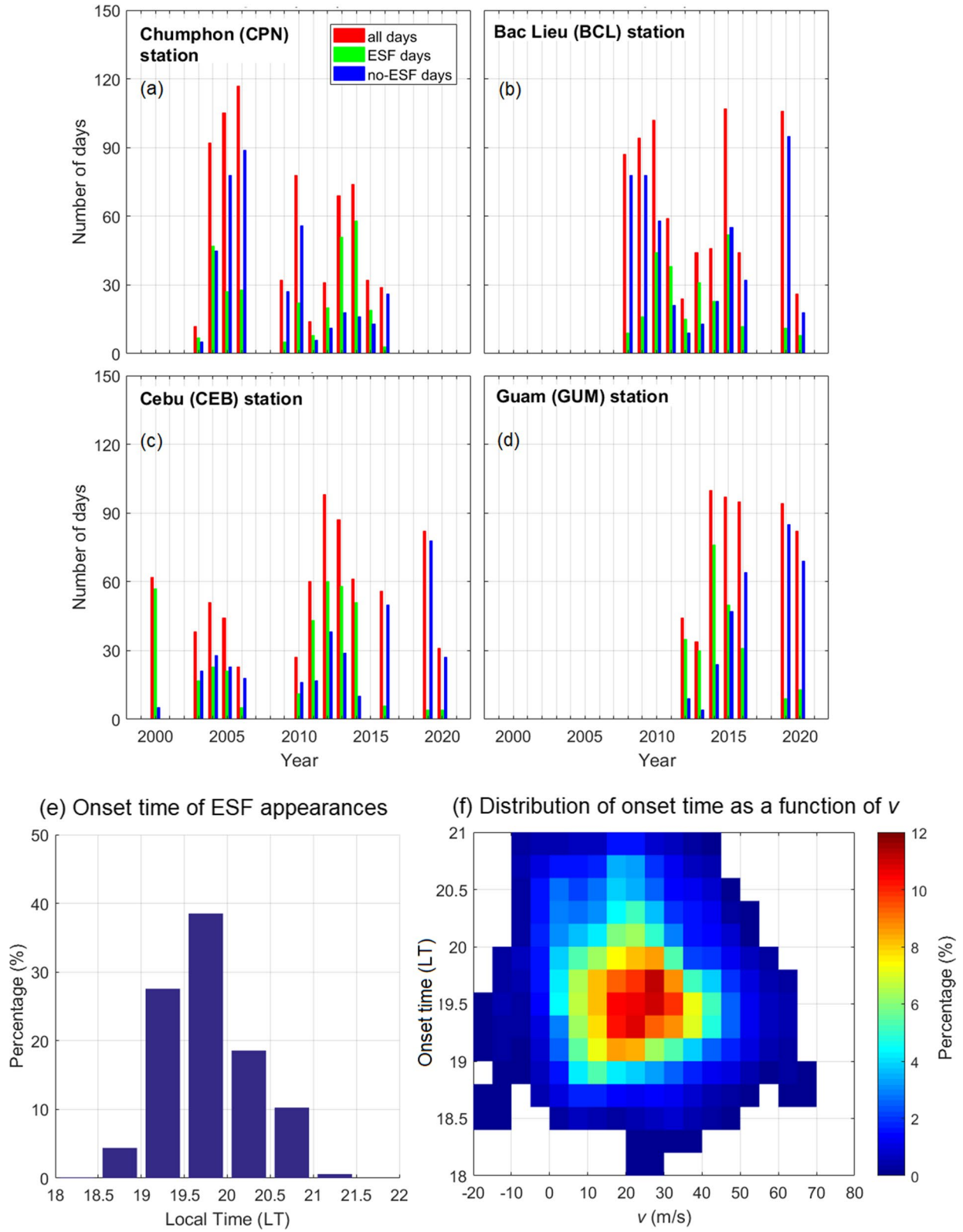

Fig. 3 Year-by-year distribution of the number of observation days for each ionosonde used in this study (**a**–**d**). Distribution of onset time for equatorial spread F (ESF) appearances (**e**), and onset time ESF classified by evening vertical drift (*v*) (**f**)

instrument. Furthermore, a key aspect of this study is to determine the effective range of an ionosonde's predictive capability for post-sunset ESF occurrence at other longitudes. To investigate this, experiments were conducted by pairing ionosondes to analyze the optimal coverage area for a single ionosonde in predicting post-sunset ESF occurrence. For each pair, one ionosonde's performance in predicting post-sunset ESF occurrence observed by another ionosonde was evaluated using the obtained P and z. Utilizing the observations from this study, six pairs of ionosondes with longitudinal separations ranging from 6.3° to 45.46° were created. Through this observational experiment, the study aims to examine how far one ionosonde can optimally predict post-sunset ESF occurrence at other longitudes in the zonal direction.

Results and discussion

The observational results of this study are presented in Fig. 4. The gray dots in the upper panel of Fig. 4 show the occurrence rate of post-sunset ESF as a function of evening vertical drift (v), which is derived from the 2690 observation days. The gray dots are calculated based on the ratio of the number of days with post-sunset ESF occurrence to the number of observation days within the intervals of $-20 \le v < -10, -10 \le v < 0,\ 0 \le v < 10,\ \ldots,$ and $60 \le v < 70$. The lower panel of Fig. 4 displays the count of observation days for each v interval. Analyzing the upper panel of Fig. 4, we observe that the occurrence rate of post-sunset ESF increases with higher v. When v is negative, the occurrence rate is almost zero, primarily indicating non-occurrence of post-sunset ESF. As v increases from 0 to 30 m/s, the occurrence rate of post-sunset ESF also rises, reaching 0.87. This suggests that stronger evening vertical drift is associated with a greater likelihood of post-sunset ESF. For v values equal to or greater than 40 m/s, the occurrence rate reaches 1, signifying that post-sunset ESF occurrence is consistently observed with significant v. This confirms a strong correlation between v and ESF occurrence (Abdu et al. 1983; Fejer et al. 1999; Smith et al. 2015).

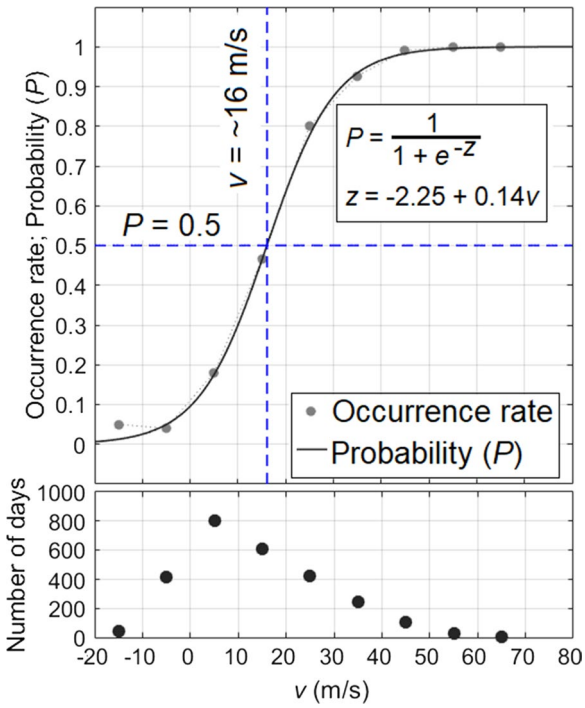

Fig. 4 The occurrence rate/probability of post-sunset equatorial spread F (ESF) as a function of the evening vertical drift (v) (upper panel). The number of data points at each interval v is displayed in the bottom panel

In the upper panel of Fig. 4, the black curve represents the logistic regression model (P and z) used to estimate the probability of post-sunset ESF occurrence as a function of v. The regression coefficients of the z-function ($\beta_0 = -2.25$ and $\beta_1 = 0.14$) were determined using the gradient descent technique. The obtained z-function was then used to calculate the probability of post-sunset ESF occurrence (P) as a function of v, and the result is shown as the black curve in the upper panel of Fig. 2. In other words, the black curve is the obtained logistic regression to model the probability of ESF occurrence (P) as a function of v, i.e., $P = 1/[1 + \exp(-z)]$ and $z = -2.25 + 0.14v$. As depicted in the figure, the black curve closely fits the gray dots representing the occurrence rate of post-sunset ESF from observations, indicating that the relationship between post-sunset ESF occurrence and v can be described by a probability function. The probability of ESF occurrence increases from zero to one as v increases from negative values to above 40 m/s. When v is negative, the probability is close to zero, indicating that ESF cannot be generated. When v is stronger than 30 m/s, the probability is greater than 0.87, indicating that ESF almost always occurs. Finally, when v is equal to or higher than 40 m/s, the probability becomes 1, indicating that ESF always occurs. This research demonstrates that the likelihood of ESF occurrence can be accurately described as a probability function with the evening vertical drift (v). As v increases, the probability of ESF occurrence rises. A velocity of 30 m/s marks the point at which the likelihood of ESF occurrence surpasses 0.87, and at v values exceeding 40 m/s, the probability reaches 1. Notably, Huang and Hairston (2015) reported that a velocity greater than 40 m/s has a probability of producing an ESF with a value greater than 0.8. The difference between our results and Huang and Hairston's can be attributed to the observation methods. While they observed ESF at altitudes above 400 km using the C/NOFS satellite, this study observed ESF from the lower ionosphere (200–300 km)

using ionosondes. Since ESF irregularities originate in the lower ionosphere and propagate upward, stronger PRE is needed to reach higher altitudes. Therefore, a PRE of 30 m/s is sufficient to generate ESF in the lower ionosphere with a 0.87 probability. In this study, a velocity of 40 m/s or greater consistently results in ESF occurrence in the lower ionosphere.

In the upper panel of Fig. 4, vertical and horizontal blue dashed lines provide a reference for evaluating the ionosonde's ability to predict post-sunset ESF occurrence using the logistic regression equations. When the probability (P) is greater than or equal to 0.5 (horizontal blue dashed line), post-sunset ESF occurrence can be expected. This corresponds to v values greater than approximately 16 m/s (vertical blue dashed line). Conversely, non-occurrence of post-sunset ESF is expected when the probability (P) is less than 0.5, i.e., when v is less than ~ 16 m/s. By following these procedures, the ionosonde's ability to predict post-sunset ESF occurrence as a function of v can be quantified and compared to observations using accuracy and the True Skill Score (TSS).

Accuracy is represented by the ratio of true positive (TP) and true negative (TN) cases over the total number of cases. TP signifies instances where both expectations and observations align in predicting post-sunset ESF occurrence, while TN corresponds to cases where both predict non-occurrence. TSS is calculated as true positive rate (TPR) − false positive rate (FPR). TPR is the ratio of TP to the number of observed post-sunset ESF occurrences, and FPR is obtained by subtracting true negative rate (TNR) from 1. TNR is the ratio of TN to the number of non-occurrences of post-sunset ESF from observation. An accuracy of over 0.7 is considered good, surpassing the accuracy of predicting ESF occurrence using the persistence technique (approximately 0.65) (Abadi et al. 2022). The persistence technique operates under the assumption that what happened on the previous day will occur on the present day or that present day conditions will persist into the next day. It serves as a baseline for comparing models, according to Carter et al. (2020). An accuracy of 0.5 indicates randomness in the relationship between ESF occurrence and v. TSS ranges from −1 to 1, with negative values suggesting false expectations, zero indicating random prediction, and positive values (even close to +1) indicate that most expectations of occurrence/non-occurrence are correctly classified by v.

Figure 5 illustrates the accuracy (black bars) and TSS (blue bars) for each ionosonde station when applying the logistic regression model found in this study, $P = 1/[1 + \exp(-z)]$ and $z = -2.25 + 0.14v$, to predict post-sunset ESF occurrence. Applying the obtained logistic regression model to the observation dataset of each ionosonde results in an accuracy of ~ 0.80 and a TSS of ~ 0.60

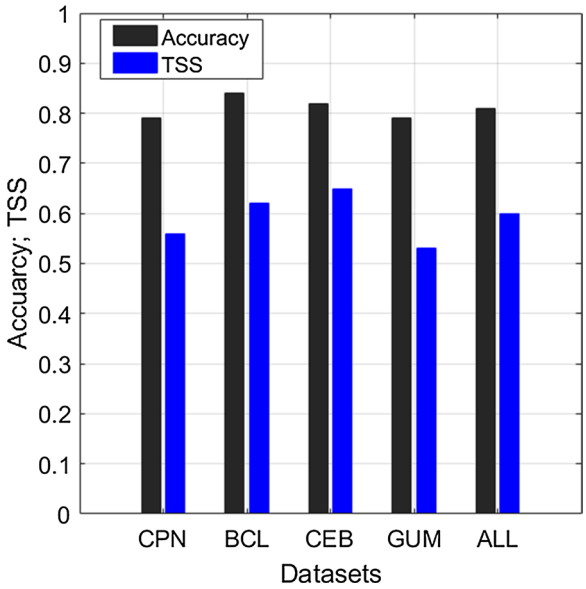

Fig. 5 Measuring performances of the obtained logistic regression model in the observation datasets using accuracy and TSS

in predicting post-sunset ESF occurrence. The logistic regression model applied to all datasets results in an accuracy of approximately 0.80 and a TSS of around 0.60 for each ionosonde. These values remain consistent when the model is applied to all datasets. This confirms that the logistic regression model developed in this study is suitable for modeling the probability of post-sunset ESF occurrence as a function of v for each ionosonde in equatorial Southeast Asia.

The following results highlight the ionosonde's predictive capabilities for post-sunset ESF occurrence at other longitudes. To investigate this, we conducted an observational experiment aimed at collecting velocity data above the ionosonde at a specific location. We employed the previously derived logistic regression model, denoted as $P = 1/[1 + \exp(-z)]$ with $z = -2.25 + 0.14v$, to forecast post-sunset ESF occurrence at different longitudes in the zonal direction. As mentioned earlier, we established pairs of ionosondes. For each pair, we computed the accuracy and TSS to assess the ability of one ionosonde to predict post-sunset ESF occurrence as observed by another ionosonde. The outcomes are detailed in Table 1, where "single station" signifies the predictive capability of an individual ionosonde directly above it, with accuracy around 0.80 and TSS approximately 0.60, as obtained from Fig. 5. The other pair combinations of ionosondes are used to evaluate an ionosonde's ability to forecast post-sunset ESF occurrence observed by a different ionosonde. For example, the CPN-BCL ionosonde pair, with a longitudinal separation of 6.30°, utilizes velocity

Table 1 Performances of ionosonde at certain stations in predicting post-sunset equatorial spread F (ESF) occurrence in different stations

Combination	Longitudinal distance	Number of days	Performance	
			Accuracy	TSS
Single station	0°	2690	0.81	0.60
CPN–BCL	6.30°	169	0.68	0.36
BCL–CPN	−6.30°		0.73	0.46
BCL–CEB	18.20°	274	0.74	0.44
CEB–BCL	−18.20°		0.73	0.43
CEB–GUM	20.96°	242	0.80	0.57
GUM–CEB	−20.96°		0.79	0.52
CPN–CEB	24.50°	248	0.67	0.33
CEB–CPN	−24.50°		0.67	0.33
BCL–GUM	39.16°	271	0.71	0.27
GUM–BCL	−39.16°		0.71	0.19
CPN–GUM	45.46°	160	0.69	0.35
GUM–CPN	−45.46°		0.67	0.38

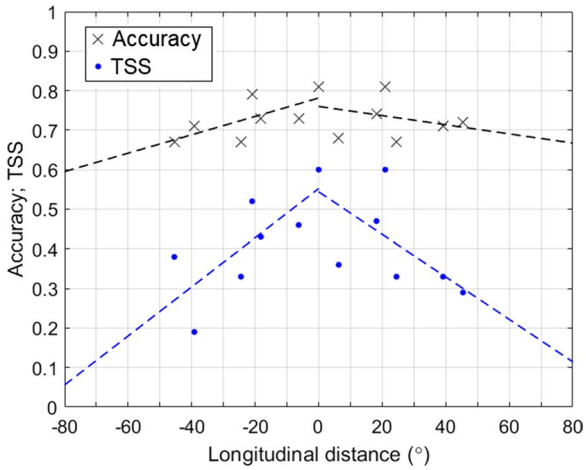

Fig. 6 Ionosonde performance in predicting post-sunset equatorial spread F (ESF) occurrence as a function of longitudinal distance

(ν) data from the CPN ionosonde to predict post-sunset ESF occurrences observed by the BCL ionosonde, located east of CPN. Conversely, the BCL-CPN pair (with a longitudinal distance of −6.30°) employs velocity data from the BCL ionosonde to predict post-sunset ESF occurrences as observed by the CPN ionosonde, located west of BCL. The third column in Table 1 specifies the number of observation days for each ionosonde pair.

Table 1 reveals that as the zonal distance between ionosondes increases, the accuracy and TSS generally diminish. Notably, the CEB-GUM/GUM-CEB ionosonde pair demonstrates notably superior accuracy and TSS compared to the BCL-CEB/CEB-BCL and CPN-BCL/BCL-CPN pairs with closer longitudinal proximity. However, this study concerns making a trend for the capability of ionosonde to predict post-sunset ESF at other longitudes. We discuss the better scores of CEB-GUM/GUM-CEB due to the random fluctuation commonly occurring in the observational experiments. In support of this interpretation, we conducted a supplementary analysis, akin to that presented in Table 1, focusing on the period from 2010 to 2015 when comprehensive data were available for each ionosonde, as depicted in Fig. 3a–d. During this supplementary analysis, accuracy (TSS) values for the CPN-BCL, BCL-CEB, CEB-GUM, CPN-CEB, BCL-GUM, and CPN-GUM pairs were 0.66 (0.31), 0.67 (0.29), 0.74 (0.17), 0.71 (0.28), 0.59 (0.17), and 0.72 (0.11), respectively. From this supplementary analysis, we can observe that the accuracy of CEB-GUM is better than CPN-BCL and BCL-CEB, but not for the TSS. The better scores for the GUM-CEB/CEB-GUM pair are not always consistent with changes in the number of observation data. We describe another example; the pair of CPN-GUM, which has the furthest longitudinal distance, has a higher accuracy value than CPN-BCL, which has the shortest longitudinal distance. The number of data points available in each pair of ionosondes could impact the calculation of accuracy and TSS. However, the supplementary analysis still supports that the accuracy and TSS generally decrease as the zonal distance between the two ionosondes increases. Consequently, we can affirm the validity of the results presented in Table 1 regarding the overarching trend of the ionosonde's ability to predict post-sunset ESF occurrence relative to longitudinal distance.

Based on the data in Table 1, we can draw a generalized conclusion about the effective coverage of a single ionosonde in forecasting post-sunset ESF occurrence in the zonal direction. Figure 6 visually represents the scatter plots of accuracy (represented by black crosses) and TSS (represented by blue dots) as functions of longitudinal distance. Dashed lines denote the accuracy/TSS trends for both the east (positive distance) and west (negative distance) directions. Accuracy and TSS at a longitudinal distance of 0° are utilized as reference points to establish trends in both the eastward and westward directions. An ionosonde performs most optimally when predicting post-sunset ESF occurrences directly above it, with an accuracy of 0.80 and a TSS of 0.60. The ionosonde remains effective in forecasting post-sunset ESF occurrences at other longitudes in both the eastward and westward directions until the longitudinal separation reaches 30° from the ionosonde's location, with an accuracy of approximately 0.70 and a TSS of about 0.30.

In this study, we delve into the rationale underpinning the 30° coverage. One hypothesis posits that it may relate to the time span of ESF period observation employed in the study. We utilized a 2-h time span, which corresponds to a longitudinal distance of 30°. To test this supposition, we conducted an additional experiment similar to that shown in Fig. 6 but focused on the time window of 19:00–20:00, as depicted in Fig. 7. In Fig. 7, we validated the occurrence of post-sunset ESFs on specific days by considering ESF observations within the 19:00–20:00 (1-h) time interval. Additionally, we classified days without ESF appearances during 19:00–21:00 LT, as well as days with ESF appearances after 20:00 LT, as days without post-sunset ESF occurrence for the analysis presented in Fig. 7. We then calculated the regression coefficients of logistic regression (β_0 and β_1), denoted as $z=-2.34+0.10v$, for this modified dataset. Subsequently, through a similar analysis to Fig. 6, the findings in Fig. 7 reveal that the optimal coverage of an ionosonde in predicting ESF occurrence in the zonal direction reduces to 10° in longitude when a 1-h time window for ESF observation is utilized. It is noteworthy, however, that the 10° coverage does not align with the 1-h time span, which should correspond to a longitudinal distance of 15°. In summary, the 30° coverage of the ionosonde, as determined in this study, may not be substantially influenced by the duration of the ESF observation period.

An alternative rationale behind the 30° coverage may be associated with the zonal structure of the pre-reversal enhancement (PRE) in the equatorial region. The PRE induces an evening vertical plasma drift (Kelley 2009). The PRE exhibits a duration of approximately 2 h around sunset local time (Woodman 1970) aligning with a longitudinal extent of 30° at the Equator. Given that the magnetic declination angle and the magnetic Equator's offset from the geographic Equator in Southeast Asia are nearly identical, the PRE structure can be described in sun-fixed coordinates with a longitudinal scale of approximately 30°. In this study, we employed the evening vertical drift (v) from the ionosonde, closely related to the PRE. Thus, we attribute the optimal ionosonde coverage for predicting ESF occurrence in this study to the substantial zonal PRE structure (~ 30°).

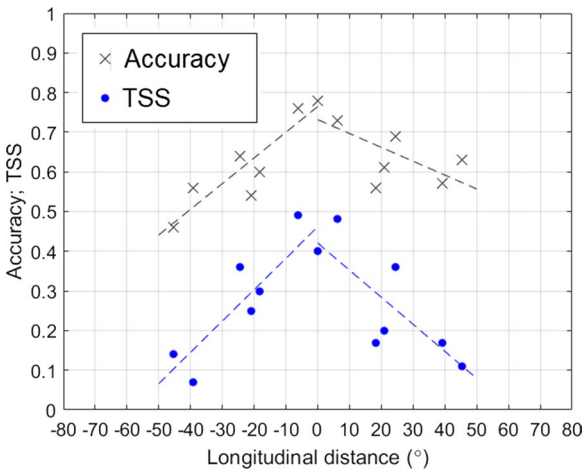

Fig. 7 Similar to Fig. 6, but in this case, the occurrence of post-sunset ESF is defined based on the time span of ESF appearance from 19:00 to 20:00 LT

Finally, this study explores the potential application of its findings to enhance operational space weather services in Southeast Asia. Post-sunset ESFs predominantly occur after sunset, and a single ionosonde in the equatorial region can forecast post-sunset ESF occurrence not only directly above the instrument, but also in longitudes to the west relative to its location since the sunset progresses westward in Earth-fixed coordinates. From a predictive standpoint, measuring vertical velocity at ionosondes located in eastern longitudes to predict post-sunset ESFs in western longitudes proves to be more effective. This approach enables the anticipation of post-sunset ESF occurrences in western longitudes while that region is still exposed to sunlight. The observational experiment in this study illustrates that each ionosonde in equatorial Southeast Asia can deliver accurate forecasts of post-sunset ESF occurrence within a longitudinal distance of up to 30° from its location. A single ionosonde can predict post-sunset ESF occurrence/non-occurrence with an accuracy of approximately ~ 0.80 directly above the instrument at least 10–15 min prior to occurrence, and it can make forecasts of post-sunset ESF occurrence/non-occurrence with an accuracy of approximately ~ 0.70 for longitudes 30° west of the ionosonde's location up to two hours before the event. These findings could significantly enhance regional space weather services.

Conclusion

This paper investigates the extent to which a single ionosonde can accurately predict the occurrence of post-sunset equatorial spread F (ESF) in the zonal direction. The study utilizes observational data from four ionosondes located near the magnetic Equator of Southeast Asia. Through the application of logistic regression analysis, the study establishes a robust relationship between the probability of post-sunset ESF occurrence (P) and the evening vertical plasma drift (v) in Southeast Asia. The value of v serves as a key determinant of the probability of post-sunset ESF occurrence, as represented by the equation $P=1/[1+\exp(-z)]$, with $z=-2.25+0.14v$. It is revealed that the probability of post-sunset ESF occurrence reaches 1 when v is greater than or equal to 40 m/s. Additionally, when v surpasses

30 m/s, the probability exceeds 0.87, signifying that post-sunset ESF almost invariably occurs. Conversely, the probability approaches zero when v is negative, indicating that post-sunset ESF generation is improbable under such conditions.

Employing the logistic regression model, the study assesses the predictive capabilities of a single ionosonde in forecasting post-sunset ESF occurrences not only directly above its location, but also across other longitudes in the zonal direction. The results demonstrate that a single ionosonde positioned at a specific location can optimally forecast the occurrence of post-sunset ESFs within a longitudinal distance of 30° from its site. The accuracy of the ionosonde in predicting post-sunset ESF occurrences directly above it stands at approximately 0.80, with a marginal decrease of 10% when forecasting post-sunset ESF occurrences at longitudinal distances of 30°.

In conclusion, this study significantly advances our comprehension of the interrelation between evening vertical plasma drift and the occurrence of post-sunset ESFs based on ionosonde observations. Moreover, it furnishes valuable insights into the optimal coverage area for ionosondes in predicting post-sunset ESF occurrences in the zonal direction. This newfound understanding can be effectively harnessed to enhance regional space weather services, thereby contributing to improved space weather prediction and management.

Abbreviations

EPB	Equatorial plasma bubble
GNSS	Global Navigation Satellite System
CPN	Chumphon station
CEB	Cebu station
BCL	Bac Lieu station
GUM	Guam station
MLAT	Magnetic latitude
SEALION	Southeast Asia Low-latitude Ionospheric Network
GIRO	Global Ionosphere Radio Observatory
EAR	Equatorial Atmosphere Radar
ESF	Equatorial spread F
MSF	Mixed spread-F
RSF	Range spread-F
FSF	Frequency spread-F
foF2	Critical frequency of ionospheric F-layer
URSI	Union Radio-Scientifique Internationale
TSS	True Skill Score
TP	True positive
TN	True negative
TPR	True positive rate
FPR	False positive rate
TNR	True negative rate
PRE	Pre-reversal enhancement
LT	Local time
v	Evening vertical plasma drift derived from ionosonde
h'	Virtual height of F-layer from ionosonde observation
P	Probability of post-sunset ESF occurrence using logistic regression
z	Linear function containing v in logistic regression
β_0 and β_1	Regression coefficients in z-function

Acknowledgements
PA, UAA, WH, and RRS are participating in this study as part of the Memorandum of Understanding for Research Collaboration on Regional Ionospheric Observation at Telkom University (No: 092/SAM3/TE-DEK/2021). The authors would like to acknowledge the SEALION and GIRO projects for providing ionosonde observations in the equatorial regions of Southeast Asia and the Pacific. The SEALION project was conducted through international collaboration by King Mongkut's Institute of Technology Ladkrabang (KMITL), Chiang Mai University (CMU), National Institute of Aeronautics and Space of Indonesia (LAPAN), Institute of Geophysics, Vietnam Academy of Science and Technology (IGP-VAST), University of San Carlos (USC), Kyoto University, Rajamangala University of Technology Isan (RMUTI), and National University of Laos (NUOL). This paper utilizes ionospheric data from the Guam station, which is part of the USAF NEXION Digisonde network, overseen by Annette Parsons, the NEXION Program Manager. The Guam station is also affiliated with the GIRO network, which provides precise electron density specifications for the Earth's ionosphere at over 60 global locations. Among these, 37 GIRO sites offer real-time ionospheric data to the central server in Lowell, Massachusetts within minutes. GIRO sites are equipped with Digisonde instruments, employing the high-frequency remote sounding technique to explore the ionosphere's bottomside from 80 km up to the peak of ionospheric plasma density. Real-time and retrospective data from GIRO locations are integrated into the Lowell Digital Ionogram DataBase (DIDBase). GIRO data are publicly accessible via DIDBase and DriftBase Web Portals, along with custom software tools for digisonde data analysis, namely SAO Explorer and Drift Explorer.

Author contributions
PA took responsibility for the conceptualization of the study, method development, software creation for data analysis, result validation, and the initial manuscript draft. Additionally, PA conducted the manuscript's review and editing. UAA, YO, PJ, AA, SP, SS, WH, and RRS contributed to the formal data analysis and participated in the manuscript review and editing. AA managed data curation and created the graphical abstract for the manuscript, while YO, UAA, and PJ handled project administration and funding acquisition. All authors have read and agreed to the final version of the manuscript.

Funding
PA would like to acknowledge the support provided by the 2022 ISEE International Joint Research and the 2023 NICT International Exchange Program. UAA would like to thank Telkom University for their support in covering the Article Processing Charge (APC) for this manuscript. AA expresses gratitude to the Manajemen Talenta of BRIN for providing the opportunity to participate in the Research Assistant Program in 2022. PJ acknowledged the financial support for this research from the Program Management Unit-Brain Power (PMU-B) through the Office of National Higher Education Science Research and Innovation Policy Council (NXPO) under grant no. B05F640197 as well as the Thailand Science Research and Innovation (Fundamental Fund, Budget year 2567 in Science Research and Innovation). This study was also supported by JSPS KAKENHI Grant Numbers 22K21345, 21H04518, and 20H00197, JSPS Bilateral Joint Research Projects no. JPJSBP120226504, and JSPS Core-to-Core Program, B. Asia-Africa Science Platforms.

Availability of data and materials
Data from the ionosondes of the SEALION and GIRO project can be accessed at https://aer-nc-web.nict.go.jp/sealion/ and https://giro.uml.edu/ionoweb/, respectively. The datasets used during the current study are available from the corresponding author upon request.

Declarations

Ethics approval and consent to participate
Not applicable.

Consent for publication
Not applicable.

Competing interests
The authors declare that they have no competing interests.

Author details
[1]Research Center for Climate and Atmosphere, Indonesian National Research and Innovation Agency (BRIN), Bandung, Indonesia. [2]School of Electrical Engineering, Telkom University, Kab. Bandung 40257, Indonesia. [3]Institute for Space-Earth Environmental Research (ISEE), Nagoya University, Nagoya, Japan. [4]Space Technology Department Center, King Mongkut's Institute Technology Ladkrabang (KMITL), Prince of Chumphon Campus, Chumphon 86160, Thailand. [5]Department of Atmospheric and Planetary Sciences, Sumatera Institute of Technology, Lampung, Indonesia. [6]National Institute of Informatics and Communications (NICT), Tokyo 184-8795, Japan. [7]Research Center for Smart Mechatronics, Indonesian National Research and Innovation Agency (BRIN), Bandung, Indonesia.

Received: 25 May 2023 Accepted: 1 December 2023
Published online: 13 December 2023

References

Abadi P, Otsuka Y, Shiokawa K, Husin A, Liu HX, Saito S (2017) Equinoctial asymmetry in the zonal distribution of scintillation as observed by GPS receivers in Indonesia. J Geophys Res Space Phys 122(8):8947–8958. https://doi.org/10.1002/2017JA024146

Abadi P, Otsuka Y, Liu HX, Hozumi K, Martiningrum DR, Jamjareegulgarn P, Thanh LT, Otadoy R (2021) Roles of thermospheric neutral wind and equatorial electrojet in pre-reversal enhancement, deduced from observations in Southeast Asia. Earth Planet Phys 5(5):387–396. https://doi.org/10.26464/epp2021049

Abadi P, Ahmad UA, Otsuka Y, Jamjareegulgarn P, Martiningrum DR, Faturahman A, Perwitasari S, Saputra RE, Septiawan RR (2022) Modeling post-sunset equatorial spread-F occurrence as a function of evening upward plasma drift using logistic regression, deduced from ionosondes in Southeast Asia. Remote Sens 14:1896. https://doi.org/10.3390/rs14081896

Abdu MA, Bittencourt JA, Batista IS (1981) Magnetic declination control of the equatorial F-region dynamo electric field development and spread F. J Geophys Res 86:11443–11446. https://doi.org/10.1029/JA086iA13p11443

Abdu MA, de Medeiros RT, Bittencourt JA, Batista IS (1983) Vertical ionization drift velocities and range type spread F in the evening equatorial ionosphere. J Geophys Res 88:399–402. https://doi.org/10.1029/JA088iA01p00399

Abdu MA, Batista IS, Sobral JHA (1992) A new aspect of magnetic declination control of equatorial spread F and F-region dynamo. J Geophys Res 97:14897–14904. https://doi.org/10.1029/92JA00826

Anderson DN, Reinisch B, Valladares C, Chau J, Veliz O (2004) Forecasting the occurrence of ionospheric scintillation activity in the equatorial ionosphere on a day-to-day basis. J Atmos Sol Terr Phys 66:1567–1572. https://doi.org/10.1016/j.jastp.2004.07.010

Booker HG, Wells HW (1938) Scattering of radio waves by the F region of the ionosphere. J Geophys Res 43:249–256

Burke WJ, Huang CY, Gentile LC, Bauer L (2004) Seasonal-longitudinal variability of equatorial plasma bubbles. Ann Geophys 22(9):3089–3098. https://doi.org/10.5194/angeo-22-3089-2004

Carter BA, Currie JL, Dao T, Yizengaw E, Retterer J, Terkildsen M, Groves K, Caton R (2020) On the assessment of daily equatorial plasma bubble occurrence modeling and forecasting. Space Weather 18:e2020SW002555

Das SK, Pavanchaitanya P, Patra AK, Niranjan K (2022) On the onset time and background ionospheric conditions of postsunset equatorial plasma bubble. J Geophys Res Space Phys 127:e2022JA030731. https://doi.org/10.1029/2022JA030731

Eccles JV (1998) Modeling investigation of the evening prereversal enhancement of the zonal electric field in the equatorial ionosphere. J Geophys Res 103(A11):26709–26719. https://doi.org/10.1029/98JA02656

Fagundes PR, Sahai Y, Batista IS, Abdu MA, Bittencourt JA, Takahashi H (1999) Observations of day-to-day variability in precursor signatures to equatorial F-region plasma depletions. Ann Geophys 17:1053–1063. https://doi.org/10.1007/s00585-999-1053-x

Farley DT, Bonelli E, Fejer BG, Larsen MF (1986) The prereversal enhancement of the zonal electric field in the equatorial ionosphere. J Geophys Res 91(A12):13723–13728

Fejer BG, Scherliess L, de Paula ER (1999) Effects of the vertical plasma drift velocity on the generation and evolution of equatorial spread F. J Geophys Res 104:19859–19869. https://doi.org/10.1029/1999JA900271

Fukao S, Hashiguchi H, Yamamoto M, Tsuda T, Nakamura T, Yamamoto M, Sato T, Hagio M, Yabugaki Y (2003) Equatorial Atmospheric Radar (EAR): system description and first results. Radio Sci 38(3):1053. https://doi.org/10.1029/2002RS002767

Huang C, Hairston MR (2015) The postsunset vertical plasma drift and its effects on the generation of equatorial plasma bubbles observed by the C/NOFS satellite. J Geophys Res Space Phys 120:2263–2275. https://doi.org/10.1002/2014JA020735

Ishii M, Shiota D, Tao C, Ebihara Y, Fujiwara H, Ishii T, Ichimoto K, Kataoka R, Koga K, Kubo Y, Kusano K, Miyoshi Y, Nagatsuma T, Nakamizo A, Nakamura M, Nishioka M, Saito S, Sato T, Tsugawa T, Yoden S (2021) Space weather benchmarks on Japanese society. Earth Planets Space 73:108. https://doi.org/10.1186/s40623-021-01420-5

Kelley MC (2009) The Earth's ionosphere: plasma physics and electrodynamics, 2nd edn. Academic Press, San Diego

Kil H, Oh S-J (2011) Dependence of the evening prereversal enhancement of the vertical plasma drift on geophysical parameters. J Geophys Res 116:A05311. https://doi.org/10.1029/2010JA016352

Kil H, Paxton LJ, Oh S-J (2009) Global bubble distribution seen from ROCSAT-1 and its association with the pre-reversal enhancement. J Geophys Res 114:A06307. https://doi.org/10.1029/2008JA013672

Li G, Otsuka Y, Ning B, Abdu MA, Yamamoto M, Wan W, Liu L, Abadi P (2016) Enhanced ionospheric plasma bubble generation in more active ITCZ. Geophys Res Lett 43:2389–2395. https://doi.org/10.1002/2016GL068145

Li G, Ning B, Otsuka Y, Abdu MA, Abadi P, Liu Z, Spogli L, Wan W (2021) Challenges to equatorial plasma bubble and ionospheric scintillation short-term forecasting and future aspects in East and Southeast Asia. Surv Geophys 42:201–238

Maruyama T, Kawamura M, Saito S, Nozaki K, Kato H, Hemmakorn N, Boonchuk T, Komolmis T, Ha Duyen C (2007) Low latitude ionosphere-thermosphere dynamics studies with ionosonde chain in Southeast Asia. Ann Geophys 25:1569–1577. https://doi.org/10.5194/angeo-25-1569-2007

Olla A, Abadi P, Srigutomo W (2020) Investigation of the latitudinal occurrence rate of ionospheric plasma bubble in case of strong and weak pre-reversal enhancement in Southeast Asia. J Phys Conf Ser 1523:012024. https://doi.org/10.1088/1742-6596/1523/1/012024

Patra AK, Das SK (2023) On the upwelling of the F layer base and prediction of equatorial plasma bubble. Geophys Res Lett 50:e2023GL102803. https://doi.org/10.1029/2023GL102803

Piggott, WR, Rawer, K (1972) URSI handbook of ionogram interpretation and reduction; Report UAG-23A, World Data Center for Solar Terrestrial Physics. NOAA, Boulder, CO

Povero G, Alfonsi L, Spogli L, Di Mauro D, Cesaroni C, Dovis F, Romero R, Abadi P, Le Huy M, La The V, Floury N (2017) Ionosphere monitoring in South East Asia in the ERICA Study. J Inst Navig 64:273–287. https://doi.org/10.1002/navi.194

Povero G, Pini M, Dovis F, Romero R, Abadi P, Alfonsi L, Spogli L, Di Mauro D, Huy Minh L, The Vinh L, Floury N (2015) Ionosphere monitoring in South East Asia: activities in GINESTRA and ERICA projects. In: 2015 International Association of Institutes of Navigation World Congress (IAIN), Prague, Czech Republic, pp 1–7. https://doi.org/10.1109/IAIN.2015.7352230

Reinisch BW, Galkin IA (2011) Global ionospheric radio observatory (GIRO). Earth Planets Space 63:377–381. https://doi.org/10.5047/eps.2011.03.001

Saito S, Maruyama T (2007) Large-scale longitudinal variation in ionospheric height and equatorial spread F occurrences observed by ionosondes. Geophys Res Lett 34:L16109. https://doi.org/10.1029/2007GL030618

Seo J, Walter T, Chiou TY, Enge P (2009) Characteristics of deep GPS signal fading due to ionospheric scintillation for aviation receiver design. Radio Sci 44:RS0A16. https://doi.org/10.1029/2008RS004077

Smith JM, Rodrigues FS, de Paula ER (2015) Radar and satellite investigations of equatorial evening vertical drifts and spread F. Ann Geophys 33:1403–1412. https://doi.org/10.5194/angeo-33-1403-2015

Su S-Y, Chao CK, Liu CH (2008) On monthly/seasonal/longitudinal variations of equatorial irregularity occurrences and their relationship with the postsunset vertical drift velocities. J Geophys Res 113:A05307. https://doi.org/10.1029/2007JA012809

Thampi SV, Yamamoto M, Tsunoda RT, Otsuka Y, Tsugawa T, Uemoto J, Ishii M (2009) First observations of large-scale wave structure and equatorial

spread F using CERTO radio beacon on the C/NOFS satellite. Geophys Res Lett 36:L18111. https://doi.org/10.1029/2009GL039887
Tsunoda RT, Saito S, Nguyen TT (2018) Post-sunset rise of equatorial F layer, or upwelling growth? Prog Earth Planet Sci 5:22. https://doi.org/10.1186/s40645-018-0179-4
Woodman RF (1970) Vertical drift velocities and east-west electric fields at the magnetic equator. J Geophys Res 75:6249–6259. https://doi.org/10.1029/JA075i031p06249
Woodman RF, La Hoz C (1976) Radar observations of F region equatorial irregularities. J Geophys Res 81(31):5447–5466. https://doi.org/10.1029/JA081i031p05447

Publisher's Note